Offshore stereo measurements of gravity waves

A. Benetazzo , F. Fedele , G. Gallego , P.-C. Shih , A. Yezzi

A B S T R A C T

Stereo video techniques are effective for estimating the space-time wave dynamics over an area of the ocean. Indeed, a stereo camera view allows retrieval of both spatial and temporal data whose statistical content is richer than that of time series data retrieved from point wave probes. To prove this, we consider an application of the Wave Acquisition Stereo System (*WASS*) for the analysis of offshore video measurements of gravity waves in the Northern Adriatic Sea. In particular, we deployed *WASS* at the oceanographic platform *Acqua Alta*, off the Venice coast, Italy. Three experimental studies were performed, and the overlapping field of view of the acquired stereo images covered an area of approximately 1100 m^2. Analysis of the *WASS* measurements show that the sea surface can be accurately estimated in space and time together, yielding associated directional spectra and wave statistics that agree well with theoretical models. From the observed wavenumber-frequency spectrum one can also predict the vertical profile of the current flow underneath the wave surface. Finally, future improvements of *WASS* and applications are discussed.

1. Introduction

The statistics and spectral properties of ocean waves are typically inferred from time series measurements of the wave surface displacements retrieved from wave gauges, ultrasonic instruments or buoys at a fixed point P of the ocean. However, the limited information content of point measurements does not accurately predict the space-time wave dynamics over an area centered at P, especially the maximum surface elevation over the same area, which is generally larger than that observed in time at P (Fedele et al., 2011; Forristall, 2006, 2007). Synthetic Aperture Radar (SAR) or Interferometric SAR (INSAR) remote sensing provide sufficient resolution for measuring waves only at large spatial scales longer than 100 m (see, e.g., Marom et al., 1990, 1991; Dankert et al., 2003). However, they are insufficient to estimate spectral properties at smaller scales. Presently, at such scales, field measurements for estimating directional wave spectra are challenging or inaccurate even if one could employ linear or two-dimensional wave probe-type arrays, which are expensive to install and maintain (Allender et al., 1989; O'Reilly et al., 1996).

Stereo video techniques can be effective for such precise measurements which are beneficial for many applications, such as the validation of remote sensing data, the estimation of dissipation rates, and gathering statistics of breaking waves for the correct parameterization of numerical wave models. Indeed, a stereo camera view provides both spatial and temporal data whose statistical content is richer than that of time series retrieved from wave gauges (Benetazzo, 2006; Fedele et al, 2012, 2011; Gallego et al., 2011). Since the water surface is a specular object in rapid movement, it is convenient to acquire stereo-pairs simultaneously, and the geometry of the stereo system is designed to minimize errors due to sea surface specularities (Jahne, 1993). Further, prior art has based the reconstruction of the water surface on epipolar techniques (Benetazzo, 2006), which find pixel correspondences in the two synchronized images via pixel-by-pixel based searches that are computationally expensive. Only in the last two decades or so, has this traditional approach to stereo imaging become suitable for applications in oceanography thanks to the advent of high performance computer processors. For example, Shemdin et al. (1988) and Banner et al. (1989) estimated directional spectra of short gravity waves, and Benetazzo (2006) proposed and optimized a Wave Acquisition Stereo System (*WASS*) for field measurements at the coast. More recently, Bechle and Wu (2011) have studied coastal waves over areas of ~3 m^2 using a trinocular system (Wanek and Wu, 2006), de Vries et al. (2011) have presented stereo measurements of waves in the surf zone over an area of ~1000 m^2, and Kosnik and Dulov (2011) have estimated sea roughness from stereo images.

In this paper, we present a new application of *WASS* for offshore stereo measurements of gravity waves over large areas of ~1100 m^2. *WASS* was deployed at the oceanographic tower *Acqua Alta* in the Northern Adriatic Sea, off the Venice coast in Italy (see Fig. 1), and video measurements were acquired in three experiments carried

out between 2009 and 2010 to investigate both the space-time and spectral properties of oceanic waves.

The paper is organized as follows. We first provide an overview of *WASS* deployment at *Acqua Alta* and then discuss the image processing behind the stereo reconstruction of the wave surface and the expected errors. We then present the statistical analysis of the *WASS* data and their validation using measurements collected by point probe-type instruments installed at the platform. Furthermore, we compare the wave statistics at a given point against theoretical models and provide estimates of the vertical profile of the current flow underneath the wave surface from the observed wavenumber-frequency spectrum. Finally, we discuss future developments and applications for *WASS*.

1.1. WASS deployment at Acqua Alta

The *Acqua Alta* oceanographic platform is located within the Northern Adriatic Sea, 10 miles off the coastline of Venice in waters 16 meters deep (45° 18.83′ N, 12° 30.53′ E). The Marine Science Institute of the Italian National Research Council (CNR-ISMAR) manages the tower (Cavaleri et al., 1997; Malanotte-Rizzoli and Bergamasco, 1983). *Acqua Alta* is equipped with a meteo-oceanographic station, which provides measurements of wind, temperature, humidity, solar radiation, rain, waves (directional), tides and sea temperature. Conventional tide and wave gauges are also operational together with a NORTEK AS AWAC Acoustic Doppler Current Profiler (ADCP) installed eastward, approximately 20 m away from the platform's legs.

WASS was permanently installed on the Northeast side of the tower in order to expose the stereo camera field of view to wave conditions caused by Breeze/Sirocco winds (blowing approximately from South-East) and Bora (blowing approximately from North-East). This configuration minimizes diffraction effects from the platform. Further, *WASS* rests approximately 12.5 m above the mean sea level on the third floor of the platform in order to maximize the ocean surface area imaged by the common field of view of the two cameras. In this setting, the stereo image pairs cover a common trapezoidal area with sides of length 30 m and 100 m, and a width of 100 m as shown in Fig. 2. The resulting imaged area is approximately 1100 m^2.

The deployed *WASS* consists of two BM-500GE JAI digital cameras (2456×2058 CCD active pixels with a square cell size of 3.45 μm× 3.45 μm, and a 8-bit based dynamical range) mounting 5-mm focal length low distortion lenses. The baseline between the two cameras is set ranging between 2.5 m and 3.0 m. The cameras are synchronized by an external trigger which allows 5, 10, and 15 Hz frame acquisition rates. The synchronization delay is kept within 1 ms as required for wave measurements (Holthuijsen, 1983). For each camera, a digital image data transfer rate up to 75 Megabyte/s is managed by a dedicated Giga Ethernet device and high performance hard drives at the acquisition workstation (see Fig. 1, right).

1.2. Stereo cameras model and calibration

The stereo reconstruction of the wave surface relies on a perspective pinhole camera model that infers 3-D world coordinates from pairs of stereo image coordinates (see, for example, Ma et al., 2004; Benetazzo, 2006). To infer the coordinates of 3-D points from their images taken from different views, four distinct Cartesian systems must be set as shown in panel (a) of Fig. 3. A global world coordinate system $\boldsymbol{X}=[X, Y, Z]^{\mathrm{T}}$ relates to the observed scene, where the superscript T denotes transposition. Here, the X and Y axes lie within the horizontal plane coincident with the mean sea level, and the orthogonal Z axis points upward toward the sky. For each camera, consider also a local coordinate system $\boldsymbol{X}'=[X',Y',Z']^{\mathrm{T}}$, where the Z' axis coincides with the camera's line of sight, viz. the line passing through the CCD's principal point and the theoretical lens focal point, while the X' and Y' axes are parallel to the CCD image axes (assuming the CCD is a perfect rectangle). The fourth coordinate system defines the 2-D image coordinates $\boldsymbol{J}=[j,i]^{\mathrm{T}}$ (in pixels) of the scene. Given a camera, the relationship between $\boldsymbol{X}'$ and $\boldsymbol{J}$ coordinates depends on the focal length, the size and shape of the CCD cell size, and the position of the CCD chip in the camera-lens system. These parameters are referred to as internal because they depend on the camera-lens coupling.

On the other hand, the so called external parameters define the orientation and displacements between the camera coordinates $\boldsymbol{X}'$ and the global world coordinates $\boldsymbol{X}$. These parameters are given by three successive rotations (ϕ, azimuth; τ, tilt; σ, roll) about the world reference system axes and three translations parallel to the same axes. In particular, for each camera the complete matrix transformation from $\boldsymbol{X}$ to $\boldsymbol{X}'$ is given by (Ma et al., 2004)

$$\begin{bmatrix}\boldsymbol{X}'\\1\end{bmatrix}=\begin{bmatrix}X'\\Y'\\Z'\\1\end{bmatrix}=\begin{bmatrix}R & \boldsymbol{B}\\0_3^T & 1\end{bmatrix}\begin{bmatrix}X\\Y\\Z\\1\end{bmatrix}=\begin{bmatrix}R & \boldsymbol{B}\\0_3^T & 1\end{bmatrix}\begin{bmatrix}\boldsymbol{X}\\1\end{bmatrix}, \tag{1}$$

where R is the rotation matrix defined by the three angles (ϕ,τ,σ), and $\boldsymbol{B}$ is the translation vector between the origins of the camera and world coordinate systems. Finally, the complete transformation from $\boldsymbol{X}$ world coordinates to $\boldsymbol{J}$ pixel image coordinates is given by:

$$Z\begin{bmatrix}j\\i\\1\end{bmatrix}=\begin{bmatrix}f_X & 0 & o_X\\0 & f_Y & o_Y\\0 & 0 & 1\end{bmatrix}\begin{bmatrix}1 & 0 & 0 & 0\\0 & 1 & 0 & 0\\0 & 0 & 1 & 0\end{bmatrix}\begin{bmatrix}R & \boldsymbol{B}\\0_3^T & 1\end{bmatrix}\begin{bmatrix}X\\Y\\Z\\1\end{bmatrix}, \tag{2}$$

where $[f_X, f_Y]^{\mathrm{T}}$ is the lens focal length vector, and $[o_X, o_Y]^{\mathrm{T}}$ is the principal position (in pixels) on the CCD plane. Here, a lens is approximated by a pin-hole through which all optical rays pass without distortions.

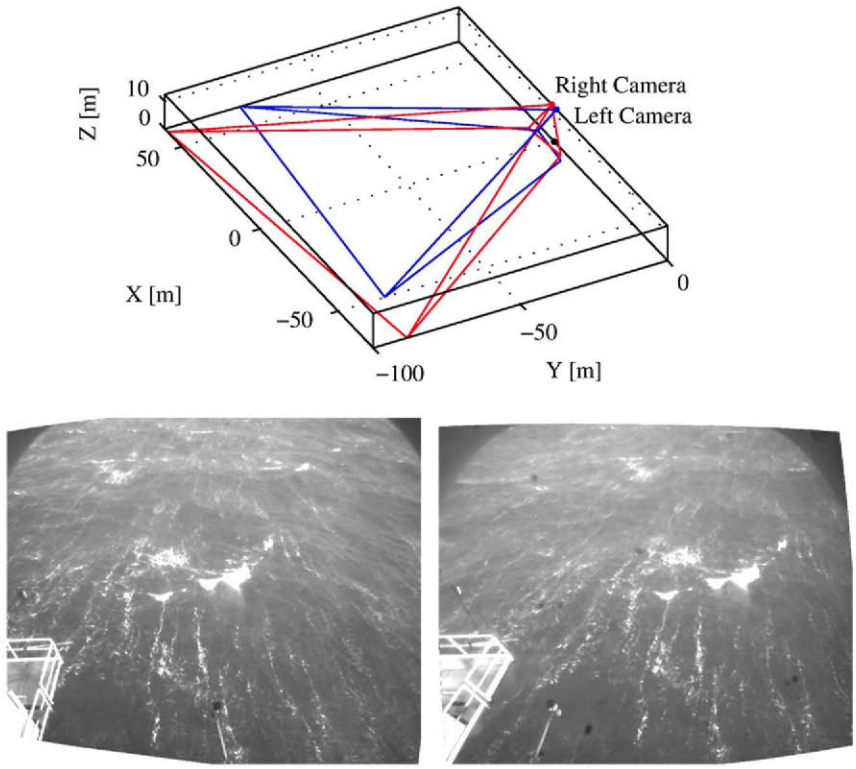

Fig. 2. *WASS* deployment at *Acqua Alta*. Top: Left (blue lines) and Right (red lines) camera fields of view. The origin of world coordinate system (*X*,*Y*,*Z*) is on the vertical projection of the Left camera principal point on the mean water surface horizontal plane. The *Y* axis was approximately set parallel to the North-East direction. Bottom: Example of synchronized images of the sea framed by Left and Right cameras.

In reality, lens optics differs from the theoretical camera pin-hole model, and pixel coordinates $[j,i]^{\mathrm{T}}$ are distorted as (Ma et al., 2004)

$$\begin{bmatrix} j_d \\ i_d \end{bmatrix} = \left[1 + k_r(1)d^2 + k_r(2)d^4 + k_r(3)d^6\right] \begin{bmatrix} j \\ i \end{bmatrix} + \begin{bmatrix} \Delta j \\ \Delta i \end{bmatrix}, \tag{3}$$

where k_r is the 3-element vector to approximate radial lens distortion, which depends on the distance d between the current pixel at $[j,i]^{\mathrm{T}}$ and that of the principal point (i.e., the origin of the $\boldsymbol{J}$ coordinates). Further, $[\Delta j, \Delta i]^{\mathrm{T}}$ is the tangential distortion vector defined as

$$\begin{bmatrix} \Delta j \\ \Delta i \end{bmatrix} = \begin{bmatrix} 2k_t(1)ji + k_t(2)\left(d^2 + 2j^2\right) \\ k_t(1)\left(d^2 + 2i^2\right) + 2k_t(2)ji \end{bmatrix}, \tag{4}$$

where k_t is the 2-element tangential lens distortion vector. Distortions can be corrected if the vectors k_r and k_t are known. For each camera,

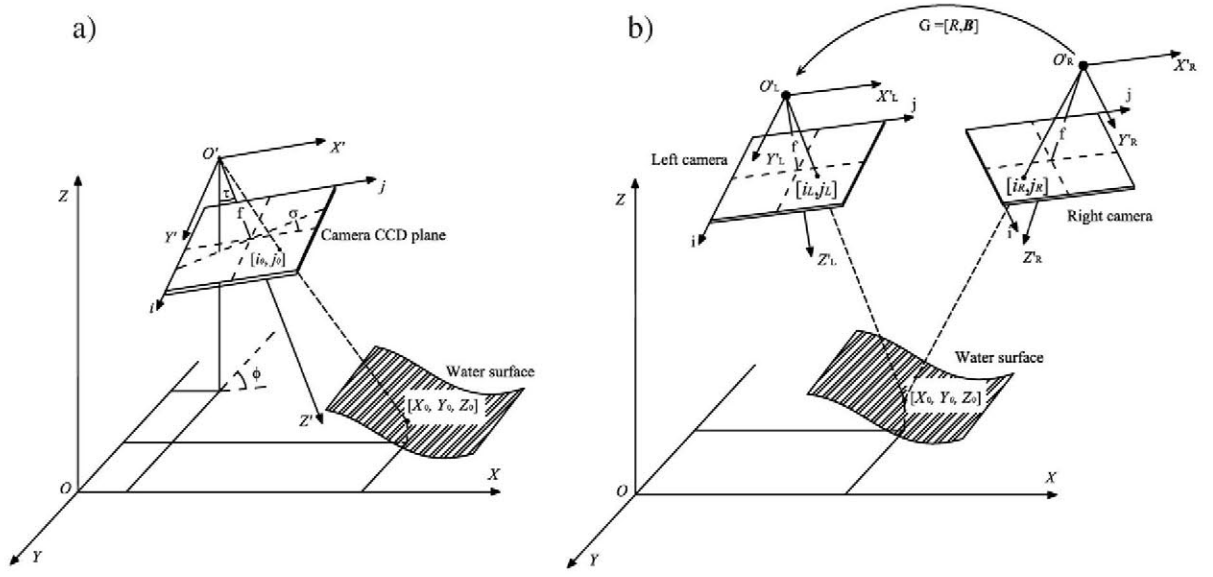

Fig. 3. (a): Relationship between the camera coordinates $[X',Y',Z']^{\mathrm{T}}$, image coordinates $[i,j]^{\mathrm{T}}$, world coordinates $[X,Y,Z]^{\mathrm{T}}$, water surface point $[X_0,Y_0,Z_0]^{\mathrm{T}}$, and rotation angles ($\phi$, τ, σ) used in the orientation definition. f is the focal length of the camera-lens system. (b): Set-up of two camera (Left and Right in Figure) stereometric intersection which allows one to determinate the three dimensions of a water surface point $[X_0,Y_0,Z_0]^{\mathrm{T}}$. $[i_L, j_L]^{\mathrm{T}}$ and $[i_R, j_R]^{\mathrm{T}}$ are the Left and Right camera coordinates of the point $[X_0,Y_0,Z_0]^{\mathrm{T}}$. $G=[\boldsymbol{R},\boldsymbol{B}]$ is the rigid transformation between Right $\boldsymbol{X}_R'$ and Left $\boldsymbol{X}_L'$ camera coordinate systems. In Figure, the camera CCD plane and the focal length f are magnified.

the intrinsic calibration (Heikkila and Silven, 1997; Ma et al., 2004; Zhang, 2000) is the procedure that allows the user to estimate the internal parameters needed in Eqs. (2)–(4), viz. the lens focal length vector $[f_X, f_Y]^T$, the principal point image coordinates $[o_X, o_Y]^T$ on the CCD plane, and the distortion vectors k_r and k_t. These parameters are summarized in Table 1 for the *WASS* cameras installed at *Acqua Alta*.

Given the two camera pixel positions $\boldsymbol{J}_L$ and $\boldsymbol{J}_R$, one can infer the 3-D coordinates of the associated world point $\boldsymbol{X}_0$ given the two 3-D rigid transformations from the world reference system to Left and Right camera reference systems, respectively. Consequently, such a geometric constraint, viz. the rigid motion between Left and Right camera reference systems, is used to triangulate image coordinates with respect to one of two image coordinates as shown in panel (b) of Fig. 3. The six degrees of freedom (three consecutive rotations and three orthogonal translations) of the 3-D rigid motion between the Left and Right cameras coordinate systems can be estimated via an extrinsic calibration procedure.

Finally, to infer the 3-D rigid motion in Eq. (2) between, say, the Left camera and the world coordinates system we assume that the time average of the mean level of the water surface elevation is a plane orthogonal to the direction of gravity, viz. Z. Benetazzo (2006) validated such assumption, which allows operating *WASS* without ground control points. Rigid motion is estimated by fitting the 3-D reconstructed surface with a mean plane $aX' + bY' + cZ' + e = 0$ in the camera reference system. Such a plane is then rotated and translated to the world camera system according to the rotation matrix R_W and the translation vector $\boldsymbol{t}_w$ given, respectively, by

$$R_W = \begin{bmatrix} 1-\dfrac{(1-c)a^2}{a^2+b^2} & -\dfrac{(1-c)ab}{a^2+b^2} & -a \\ -\dfrac{(1-c)ab}{a^2+b^2} & 1-\dfrac{(1-c)b^2}{a^2+b^2} & -b \\ a & b & c \end{bmatrix} \tag{5}$$

$$t_w = [\,0, 0, e]^T \tag{6}$$

where a, b, c, and e are the mean plane parameters. The estimation is made robust by averaging several thousand mean planes calculated from all the stereo snapshots within the given time sequence. As an example, Fig. 4 shows a time sequence of images (snapshots) taken by *WASS* and the associated elevation maps of the wave surface reconstructed by stereo-matching of pixels within the red box.

1.3. Image processing and expected errors

The epipolar algorithm herein proposed is a local method since each pixel correspondence is processed independently from the other pairs. Consequently, the resulting reconstructed wave surface is a collection of 3-D scattered points, and proper interpolation enforces spatial and temporal continuity (Benetazzo, 2006). The key issue in such methods is the optimal selection of both the Aggregation Support Window (ASW) and Search Area (SA) for pixel matching with respect to the 2-D image coordinates $[i,j]^T$ (Tombari et al., 2008). Since the camera parameters are known, epipolar geometry reduces the 2-D search to a sequence of 1-D searches along epipolar lines (or a band to account for uncertainties). For example, choose the pixel (point) denoted by the blue dot in the Right image shown in Fig. 5. The most likely matching point in the Left image is sought within an area smaller than the entire left image (blue dashed rectangle in Fig. 5) based on a weighted normalized cross-correlation (CC) between the image content delimited by the Left and Right ASWs centered at the generic matching point (red dot) and the fixed pixel (blue dot) respectively. For *WASS*, the weight or CC kernel to perform convolution is chosen as an elliptical Gaussian (Nobach and Honkanen, 2005). A CC map, such as that shown in Fig. 6, is then computed from the CC value at each pixel as the Right ASW spans all the pixels within the Left SA (convolution). Since noisy images usually yield low cross-correlations, we select the pixel position of the maximum M of the CC map as the most probable matched pixel if $M > 0.85$ (blue dot in the left panel of Fig. 5). This guaranties a good balance between reliability of pixel correspondences and the total number of matched pixels, thereby reducing unmatched spots. Moreover, if the second-to-first peak ratio of the CC map exceeds 0.6, we discard the matched pixel in order to avoid mismatching when periodic patterns occur in the SA.

As a result, the matching procedure described above yields a dense disparity map, viz. the map of the differences in position (displacements) of corresponding pixels along the rectified j axis. However, this map is not continuous since some pixels correspondences are discarded because of low CC, or because marked as spikes. Before triangulation, we use a three-point time interpolation to average an actual disparity map with those before and after in the time sequence. This enforces the spatial and temporal continuity of the wave surface reducing unmatched regions of the disparity map.

We point out that the sizes of both the ASW and SA affect the robustness, uniqueness and matching of corresponding pixels and therefore the accuracy of the disparity map. First, smaller ASWs produce unwanted noisy disparities. On the other hand, larger ASWs lead to smoother disparity maps that are, however, too computationally expensive to obtain even when the convolution is performed via the Fast Fourier Transform (FFT). Indeed, on a dual processor in MATLAB© the convolution of an ASW with size 40×80 pixels in a SA of 60×130 pixels takes 0.01 s. Doubling the size quadruples the computational time. In our experience, the optimal ASW size is approximately 40×80 pixels. Moreover, the SA size depends upon the *WASS* geometry. In particular, if the camera separation, the matched area, or the wave surface amplitude is large, the SA must be as well.

To maximize the accuracy of disparities, in contrast to the multi-resolution method proposed by Benetazzo (2006) we have adopted a two-step iteration approach that compromises between computational efficiency and uniqueness as well as reliability of the pixel matching. For the *Acqua Alta* data, a first estimate of the sea surface and the associated mean plane is obtained by matching 200 pixels uniformly distributed over the matched field of view (~1200×1200 pixels) for any snapshot within the entire video sequence. At this first stage, pixel correspondences are found using an initial SA of 200×200 pixels in order to obtain a first order approximation of the disparity map at any sampled time. The minimum and maximum disparity values attained within this approximation are used to redefine a smaller SA that encompasses the possible disparities within the video sequence. Note that the approximation of the mean sea surface is computed by averaging the mean planes estimated by triangulation from each stereo pair within the video sequence. In a second iteration, denser disparity maps are computed using the resized SA centered at the corresponding pixel matched with the estimated mean sea surface. However, the final estimate of the stereo reconstructed wave surface is still affected by the following errors:

- Quantization error. Quantization is unavoidable in traditional stereo-based reconstruction. It depends on the discretization of the continuous world operated by the discrete CCD cell size. Estimates of such errors for a given stereo setup and integer values of

Table 1
WASS deployment at *Acqua Alta*: left and right stereo cameras internal parameters after calibration.

	Left camera	Right camera
Focal length vector (pixel)	[1450, 1451]	[1446, 1448]
Focal length vector (mm)	[5.0, 5.0]	[5.0, 5.0]
Principal point o (pixel)	[1217, 1063]	[1220 1069]
k_r	[−0.0299, 0.0467, 0.0000]	[−0.0431, 0.0681, 0.0000]
k_t	[−0.0007, 0.0012]	[−0.0004, −0.0001]

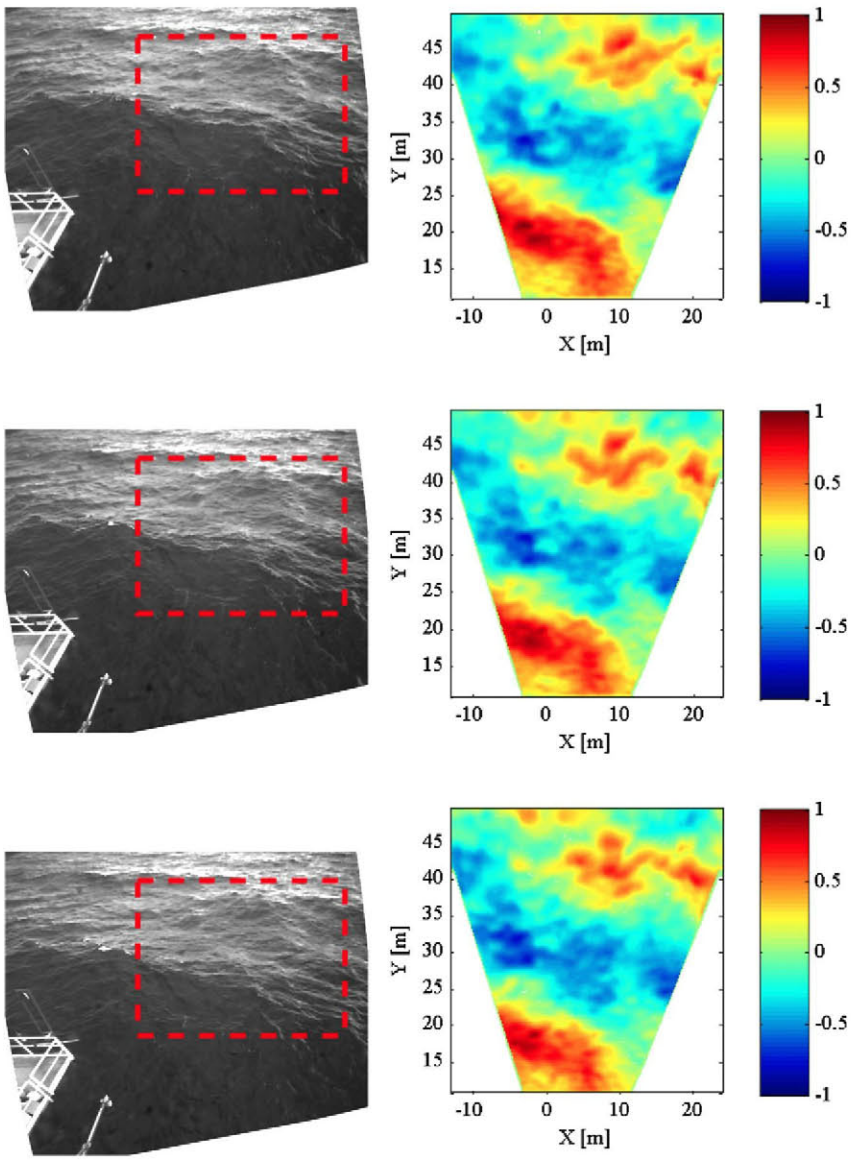

Fig. 4. *WASS* measurements at *Acqua Alta*: (left column) time sequence ($\Delta t = 2$ s) of snapshots framed by *WASS* (Left camera), and (right column) the elevation maps of the associated stereo reconstructed water surface displacements (in meters) in the world coordinate system.

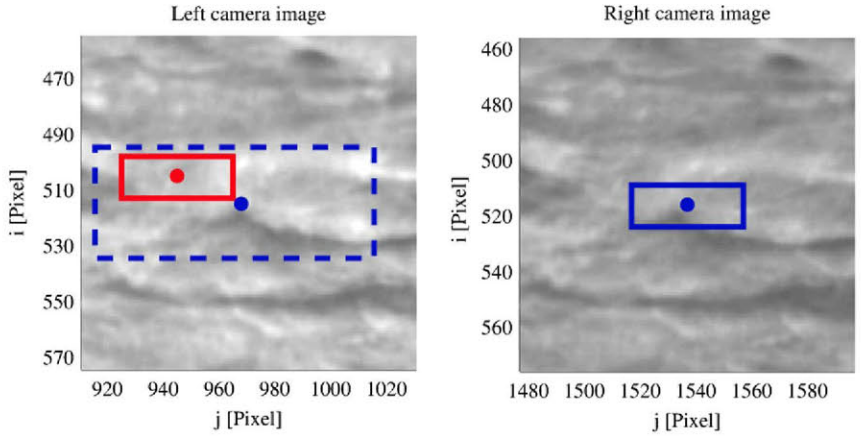

Fig. 5. Corresponding pixels (blue) between synchronous Left and Right camera images as taken by *WASS*. The blue point in the Left image is the matched pixel identified within the Search Area (dotted blue line) with the highest cross-correlation. This is computed via convolution of the two images within the left (red) and (blue) Aggregation Support Windows.

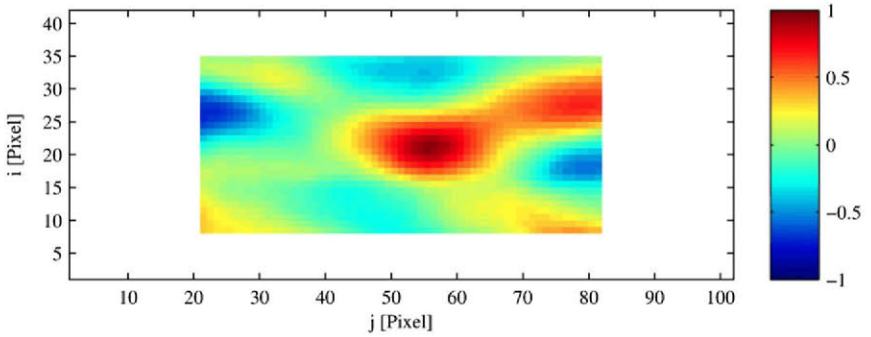

Fig. 6. *WASS* window-based stereo algorithm. Example of 2-D normalized cross-correlation map.

corresponding pixels can be found in Benetazzo (2006), Rodriguez and Aggarwal (1990) and references therein. In practical applications, quantization errors could lead to a very poor estimate of the wave surface if inferred directly from the raw integer-pixel disparity map processed based on the peak of the cross-correlation map. If the matching algorithm does not support sub-pixel accuracy of the locations of corresponding points, the resulting disparity maps will be quantized, i.e., they will show contouring effects from discontinuous transitions between regions of different disparity when pixel locations are rounded to integers. This leads to inaccurate wave surface reconstructions after triangulation, forcing the reconstructed 3-D points to lie only on a certain discrete collection of depth planes from the cameras. To mitigate this problem, a sub-pixel position estimator can be adopted to enhance the accuracy of the triangulations for the reconstructed wave surface. The difference between the true (unknown) 3-D position of a point of the wave surface and that inferred via stereo matching is the quantization error. Assuming a perfect calibration, an estimate of such an error follows by approximating the true unknown wave surface points by those estimated after sub-pixeling. Fig. 7 shows the wave elevation map error (Left panel) given by the difference between the maps estimated with and without sub-pixeling. Observe that quantization amplitude jumps of ~0.05 m. In the right panel of the same Figure, we also compare the wavenumber omnidirectional spectra associated to the two maps. As a result, quantization biases wavenumbers greater than about 7 rad/m, which corresponds to a wavelength of approximately 1 m equal to the average length of the quantization jump (see left panel of Fig. 7). Sub-pixeling reduces RMS errors depending on the weight function adopted to estimate the cross-correlation map (Nobach and Honkanen, 2005). In our case, using an elliptical Gaussian the accuracy increases by roughly a factor of 10. However, quantization errors can be large if the calibration is not perfect as shown below.

- Calibration errors. Intrinsic calibration is not as challenging as the calibration processes for the estimation of the external parameters. Indeed, internal parameters for each camera can be accurately calibrated in a controlled environment (e.g., in the laboratory) before deployment at the field site. At this first stage, the associated errors are practically null. Instead, extrinsic calibration is performed at the field site, where the logistics of the facilities and weather uncertainties can lead to highly uncontrolled conditions. Consequently, errors arising during this phase deeply affect the quality of the stereo reconstructions. To gain an understanding of such uncertainties, consider the virtual stereo setup shown in Fig. 8, where the two stereo cameras mount a 3.45-μm-CCD cell and a 5.0-mm-focal-length lens. The two camera coordinate systems are set parallel (R in Eq. (1) degenerates to the identity matrix) and 3.0 m apart in the X direction. In the common field of view, the $[X,Y,Z]^T$ position of 3-D points lying on the XY plane ($Z=0$) can be computed via triangulation from the corresponding pixels of such points in both the Left and Right cameras. For each point, the difference between the true 3-D position and that inferred via stereo matching is the quantization error discussed above. Root Mean Square (RMS) values of these errors without sub-pixel improvement are equal to $RMS_X=0.05$ m, $RMS_Y=0.16$ m, and $RMS_Z=0.05$ m along the X, Y, and Z axes, respectively. Errors in Y are larger because along this direction the pixel footprint is enlarged by the stereo projection. A uniform bias of 0.02° in the rotation angles between the two camera reference systems yields error increases up to $RMS_X=0.13$ m, $RMS_Y=0.38$ m, and $RMS_Z=0.13$ m. Instead, uniformly biasing the three components of the translation vector by 0.01 m yields $RMS_X=0.07$ m, $RMS_Y=0.20$ m, and $RMS_Z=0.07$ m. If both the biases are

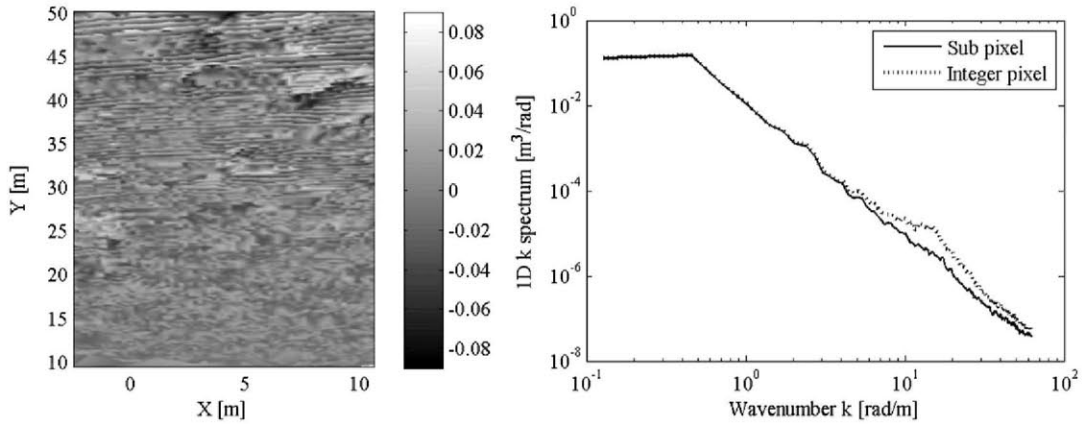

Fig. 7. Quantization errors and sub-pixeling effects in the 3-D reconstruction of the water surface. Left panel: 2-D map of the difference between the wave surface elevations estimated with and without sub-pixeling. Right panel: wavenumber spectra of the associated wave surface elevations before (dotted line) and after sub-pixeling (thick line).

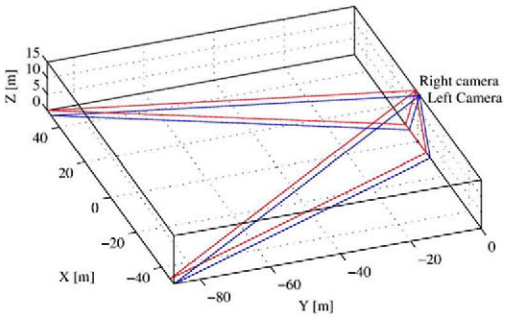

Fig. 8. Stereo setup used to simulate 3-D shape errors due to external parameters bias after calibration. Blue and red lines depict the Left and Right camera fields of view respectively. Cameras were considered mounted 15 m above the *XY* plane, and inclined of 40° with respect to this plane. Common Field of view allows one to corresponding pixel up to 80 m from the camera CCDs. Cameras separation is 3.0 m.

applied simultaneously, errors increase to $RMS_X = 0.17$ m, $RMS_Y = 0.49$ m, and $RMS_Z = 0.18$ m.

- Image regions with poor textures. The image intensity constraint is useless in textureless regions, such as bright areas due to white capping. As a result, unmatched spots occur in the reconstructed wave surface. To reduce their occurrence, and thus improve the likelihood of matched pixels, a remedy is to diffuse the image content of highly textured regions to textureless regions by spatial smoothness constraints. Moreover, the main assumption in our stereo reconstructions is that the scene of view is assumed Lambertian (Jahne, 1993). In reality, spots of specularities, reflective surfaces, or transparency can occur. Unfortunately, the variance of their gray values is not small enough to mark such regions as textureless. Indeed, even a high CC threshold in pixel matching will not avoid the effects of reflections, which alter pixel correspondences. Local optimal paths (Park and Park, 2001) and local 3-D water wave continuity (Gallego et al., 2011) can be exploited to overcome such source of errors.
- Noise. There are always unavoidable light variations, image blurring, effects of the modulation transfer function (Jahne, 1993), and sensor noise in image formation on the camera CCD. Such effects when properly modeled should be somewhat accounted for in the stereo reconstruction algorithm. For sea surface measurements, Gallego et al. (2011) have been able to include the spatial-temporal continuity of propagating waves into the stereo estimation in a global variational setting. Finally, a proper choice of the video acquisition hardware is fundamental to guarantee camera CCD gains as close as possible to zero in order to increase the number of cross-correlations and to limit unwanted mismatching which results in spikes polluting the disparity map. In our *WASS* applications, we draw from Goring and Nikora (2002) to remove unwanted spikes.

2. Data analysis

2.1. Validation of 3-d wave measurements at Acqua Alta

We acquired stereo video sequences in three experimental studies at *Acqua Alta* during 2009–2010 under both Bora and Sirocco wave climate conditions as shown in Table 2. In the same Table, for each experiment, we also report the acquisition starting date, the sequence duration, the number of acquired frames, and the associated rate. The selected matched area is approximately 1100 m^2 (*X*, *Y*, and *Z* axes oriented as in Fig. 2), and the geometrical features of the stereo photographic layout for *WASS* are given in Table 3. Expected RMS errors due to quantization for the matched area (Blostein and Huang, 1987; Rodriguez and Aggarwal, 1990; Solina, 1985) are also reported. First, we estimate quantization errors assuming a perfect calibration, so that the true unknown 3-D position of points of the wave surface is approximated by the results after sub-pixeling. As discussed in the previous section, sub-pixeling is beneficial in reducing such errors if pixel displacements are not fixed to integer values. For *WASS*, the corresponding pixel position is known up to 0.1 pixels with good approximation and quantization errors reduce roughly to ~0.01 m assuming perfect calibration conditions. In reality, calibration is not perfect and the true quantization error can be much larger, but its estimate is far from trivial since the true wave surface is unknown. For example, if we randomly alter by 3% the estimated external calibration parameters (assumed as the true values) the quantization error increases up to roughly 0.16 m as shown Table 3.

Table 2
2009–2010 *WASS* stereo experiments at *Acqua Alta* oceanographic platform. Direction angle Dir is direction where the wind comes from, measured clockwise from geographic North.

Exp #	Wind [m/s, Dir]	Starting date and hour	Frame rate [Hz]	Frames #	Duration [s]
1	6.5, 133.0 Sirocco Breeze	2009/06/05 1428 UTC	10	6000	600
2	9.6, 51.2 Bora	2009/10/14 0755 UTC	10	21000	2100
3	17.9, 67.5 Bora	2010/03/09 1120 UTC	5	9000	1800

The three experiments covered a broad range of wave conditions as shown in Table 4. Here, T_p is the peak wave period, and the steepness ε is defined as the ratio between the significant wave height H_s and the average wavelength L_m estimated from the average zero-crossing period T_z via linear dispersion (water depth $d = 16$ m). Experiment 3, with a much higher wind speed, exhibited the largest H_s / L_m ratio among the three imaged wave fields, and the acquired videos confirmed the occurrence of widespread breaking. The stereo reconstruction of the wave surface yields a three-dimensional (3-D) manifold $Z = \eta(X,Y;t)$ defined on a space-time volume V with sides $X_{max} = 35$ m, $Y_{max} = 35$ m and $t_{max} \sim 30$ min along X,Y and t, respectively. As an example, horizontal and vertical projections of the wave surface manifold from Experiment 2 are shown in Fig. 9.

WASS estimates are validated against reference point time series measurements of the wave surface elevation provided by instruments available at *Acqua Alta* including wired wave gauges and an AWAC ADCP profiler. The gauge accuracy is ~1 cm with sampling frequency of 4 Hz, whereas AWAC exhibits accuracies of 1 cm and 2° in wave elevation and direction, respectively, with sampling rate of 2 Hz. The comparisons are performed as follows: we select several virtual point probes within the reconstructed area (Bottom-left of Fig. 9) in order to extract the associated time series of the stereo-estimated wave surface displacements (Bottom-right of Fig. 9). From these, we compare various statistical and spectral properties of the waves against those obtained from *Acqua Alta* instruments, hereafter labeled as CNR. Table 5 reports these comparisons for Experiments 1, 2 and 3. Here, H_{max} is the largest wave surface height, and the peak period T_p is relative to the spectral peak of the frequency spectrum. Estimates of the significant wave heights H_{m0} and $H_{1/3}$, and wave periods T_m and T_z follow from a zero-crossing analysis of the extracted time series low-pass filtered at roughly 2.0 Hz. Clearly, such comparisons for different wave conditions show that the accuracy of *WASS* measurements is comparable to that of more traditional wave instruments since the differences between *WASS* and CNR estimates are of the order of 1–2 cm.

2.2. Wave spectra

Mean frequency spectra $S(f)$ are computed by averaging the spectra calculated from surface displacement time series at 40 virtual probes within the *XY* plane (see Fig. 9). As an example, Fig. 10 reports the estimates of $S(f)$ and the associated non-dimensional saturation

Table 3
WASS experiments at *Acqua Alta*, photographic layout and expected quantization errors: τ is the mean pitch angle of stereo cameras with respect to the horizontal plane, h is the height of the stereo baseline from the mean sea level, B is the distance between the Left and Right camera principal points, and Z_0 is the mean distance between the stereo cameras baseline and the matched area at the water surface. RMS are the root mean square expected errors of the final 3-D measurements after sub-pixeling assuming (1) perfect calibration and (2) 3% random alteration of the estimated calibration parameters (assumed as the true values).
(1) Perfect calibration, (2) imperfect calibration.

Exp #	Pitch τ [°]	h [m]	B [m]	B/Z_0	$RMS_X^{(1)}$ [m]	$RMS_Y^{(1)}$ [m]	$RMS_Z^{(1)}$ [m]	$RMS_X^{(2)}$ [m]	$RMS_Y^{(2)}$ [m]	$RMS_Z^{(2)}$ [m]
1	47.7	12.5	~3.0	0.10	0.01	0.02	0.01	0.03	0.14	0.08
2	45.8	12.5	~3.0	0.11	0.01	0.02	0.01	0.04	0.15	0.09
3	49.3	12.5	~2.5	0.09	0.01	0.02	0.01	0.05	0.16	0.10

spectrum for Experiment 2. An inertial range is seen to decay as f^{-4} in agreement with Zakharov's theory (Zakharov, 1999). However, a noise floor is noticed approximately above 2.5 Hz, and this clouds the f^{-5} Phillip's regime that should be observed due to breaking and dissipation (Newell and Zakharov, 2008; Phillips, 1977). The mean directional spectrum $S(k_X,k_Y)$ is obtained by averaging the 2-D Fourier Transforms of the reconstructed sea surface snapshots. Fig. 11 (left and center panels) shows the omnidirectional spectrum $S(k)$ that proceeds by numerically integrating $S(k_X,k_Y)$ over all directions. An inertial range that decays roughly as $k^{-2.5}$ is noted in agreement with the weak-wave turbulence of Zakharov (1999) and experiments of Hwang et al. (2000). The associated saturation spectrum (right panel of Fig. 11) shows that the tail decays with a power greater than 2.5 for wavenumbers above 3 rad/m. Some noise appears approximately above 10 rad/m, and the Phillips's regime is not observed. Severe weather conditions occurred during the video acquisition for Experiment 3, causing most probably wind-induced vibrations of the platform and stereo rig. Indeed, the estimated mean frequency spectrum $S(f)$ shows two resonant peaks above 1.0 Hz (see Fig. 12).

The 3-D wavenumber-frequency spectrum $S(k_X,k_Y;\omega=2\pi f)$ can be estimated by Fourier transforming the entire three-dimensional $Z=\eta(X,Y;t)$ wave surface data both in space and time. Two orthogonal projections (slices) of the 3-D spectrum onto the planes $k_X=0$ and $k_Y=0$ are shown in Fig. 13. Note that the regions of non-zero amplitude identify the wave dispersion curve, from which the vertical profile of the current flow velocity underneath the wave surface can be estimated as follows.

From AWAC measurements available during Experiment 3, the underwater current was directed mostly along the North direction s, and it varies with depth as shown in Fig. 15. In order to estimate currents from *WASS* data, we extract a slice of the 3-D spectrum along the direction s as shown in Fig. 14. The estimated k–ω spectrum smears out around the observed dispersion relation curve because of the well-known spectral leakage due to the finite extension of the data sets (see also Krogstad and Trulsen, 2010). Below the spectral peak, the observed dispersion curve deviates from the theoretical linear counterpart with no current (black line), viz.

$$\frac{\omega}{k}=\pm\sqrt{\frac{g}{k}} \tag{7}$$

showing a weak linear branch in the low-frequency range corresponding to a uniform speed ~0.4 m/s. Krogstad and Trulsen (2010) observed similar deviations in simulated spectra of the Dysthe equations, and according to them, it is an unexpected effect of the spectral leakage. Above the spectral peak, the Doppler-shift causes the observed wave dispersion to deviate from its linear counterpart (7). Such deviations can be related to the unknown current speed profile $U(z)$ using the modified dispersion relation (see, for example, Phillips, 1977; Boccotti, 2000)

$$k=\frac{(2\pi f-U_0k)^2}{g}, \tag{8}$$

which accounts for a uniform current U_0 collinear with the direction of wave propagation. Here, U_0 is an average speed that accounts for the effects of long-wave modulation on short waves and the variability of current with depth (Stewart and Joy, 1974). Further, U_0 is a function of k via $U(z)$ since longer waves are affected by current flows near the sea bottom, whereas shorter waves are affected by currents near the surface, viz. (Stewart and Joy, 1974)

$$U_0(k)=2k\int_{-\infty}^{0}U(z)\exp(2kz)dz. \tag{9}$$

Table 4
Wave conditions during the *WASS* experiments at *Acqua Alta*. H_s: Significant wave height, T_p: peak wave period, T_z: zero up-crossing period, L_m: mean wave length and ε: steepness. Estimates of parameters follow from measurements taken by wired wave gauges and AWAC ADCP profiler operational at *Acqua Alta*.

Exp #	Date	H_s [m]	T_p [s]	T_z [s]	L_m [m]	ε
1	2009/06/05	0.47	4.34	2.91	13	0.03
2	2009/10/14	1.09	4.59	3.51	19	0.06
3	2010/03/09	2.16	6.37	4.62	33	0.07

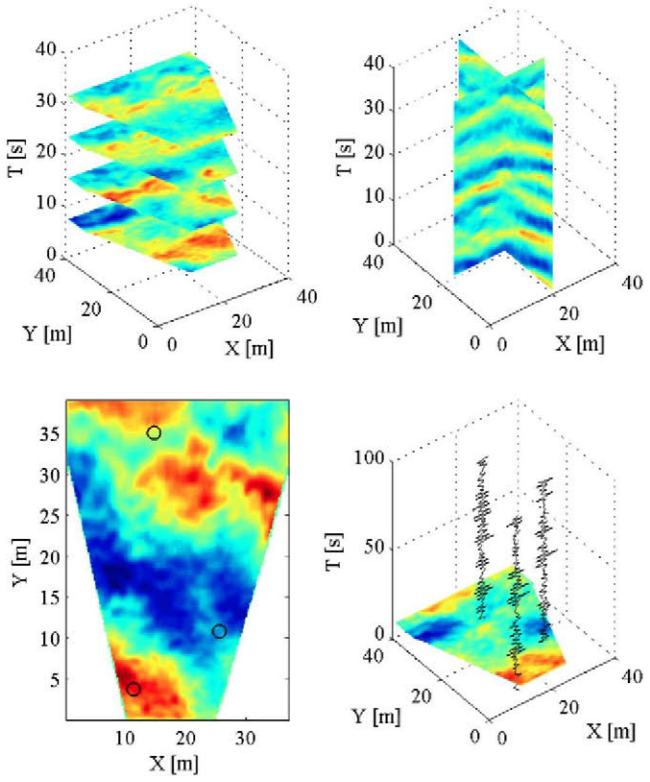

Fig. 9. Experiment 2: 4-D space-time wave volume V. Top-left: Horizontal slicing of V (sequence of snapshots). Top-right: vertical slicing of V. Bottom-left: some of the virtual probes (black circles) on the XY plane used to validate *WASS* measurements, Bottom-right: Extracted wave time series at given virtual point probes.

Table 5
Wave parameters estimated from both *WASS* instruments operational at *Acqua Alta*. *Dir* is the mean wave direction of propagation, measured clockwise from geographic North (wave directions depend upon the platform orientation that is known with an error ~3°). During Experiment 1, H_{m0}, $H_{1/3}$, and *Dir* were not available at *Acqua Alta*.

		H_{m0} [m]	$H_{1/3}$ [m]	H_{max} [m]	T_p [s]	T_z [s]	*Dir* [° N]
Exp 1	CNR	–	0.47	0.68	–	2.91	–
	WASS	0.45	0.41	0.83	4.34	3.09	148.5 ± 3
Exp 2	CNR	1.13	1.09	2.03	4.59	3.51	65.0 ± 3
	WASS	1.15	1.10	2.18	4.83	3.62	59.5 ± 3
Exp 3	CNR	2.23	2.16	3.80	6.37	4.62	69.7 ± 3
	WASS	2.17	2.16	3.95	6.36	4.85	70.1 ± 3

Estimating the profile $U(z)$ from Eqs. (8) and (9) is an ill-posed inverse problem that requires regularization. To do so, we add the constraint of an exponential profile and express U as

$$U(z) = U_{\max}\exp(\gamma z), z \le 0, \tag{10}$$

and from Eq. (9) it follows that

$$U_0(k) = \frac{2kU_{\max}}{2k+\alpha}. \tag{11}$$

Here, $k(f)$ is a function of the frequency $f = \omega/2\pi$ via the theoretical dispersion relation (8). The best values for $U_{\max}$ and α that match the observed dispersion curve (Fig. 14) with the theoretical form Eq. (8) are estimated as $U_{\max} = -0.45$ m/s and $\gamma = 0.1\ \mathrm{m}^{-1}$ respectively. The *WASS* estimate of the current profile follows from Eq. (10) and it is shown in Fig. 15 in comparison to that measured by the AWAC instrument operational at *Acqua Alta*.

2.3. Wave statistics

To study the statistical properties of waves, from Experiment 3 we consider the time series of the stereo reconstructed wave displacements extracted at several virtual probes shown in Fig. 9. The time series are filtered above 1.0 Hz to remove the noise floor observed in the associated frequency spectra, with variations less than 0.5% in the wave variance. Fig. 16 reports the empirical wave height distribution, which is in fair agreement with the Boccotti asymptotic form given by (Boccotti, 2000; Tayfun and Fedele, 2007)

$$P(H > h) = c\ \exp\left(-\frac{h^2}{4\sigma^2(1+\psi*)}\right), \tag{12}$$

where the parameters c and ψ^* both depend upon the first minimum of the wave covariance. In particular, their mean values over the time series ensemble are $c \approx 1$ and $\psi^* \approx 0.694$. Further, the observed crest/trough statistics are compared against the Tayfun–Fedele (TF) and Forristall (F) models. The TF distributions for crest (C) and trough (T) heights are given, respectively, by (Fedele, 2008; Tayfun and Fedele, 2007)

$$P(C > h) = \exp\left(-\frac{Z_c^2}{2}\right)\left(1 + \frac{\Lambda}{64}z^2\left(z^2 - 4\right)\right) \tag{13}$$

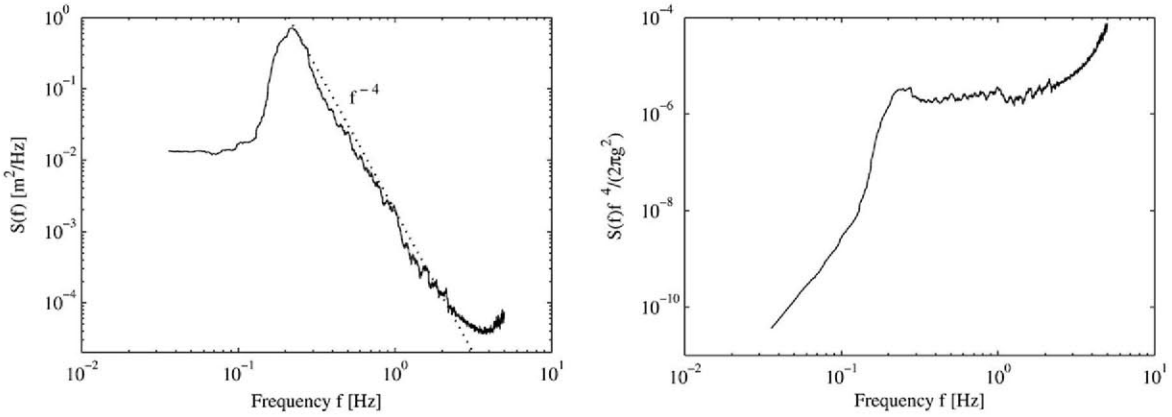

Fig. 10. Experiment 2. Left: Observed mean frequency spectrum $S(f)$ estimated from time series extracted at 40 virtual probes within the imaged area (see Fig. 9). Nyquist frequency = 5.0 Hz. Right: Associated saturation spectrum $S(f)f^4/(2\pi g^2)$.

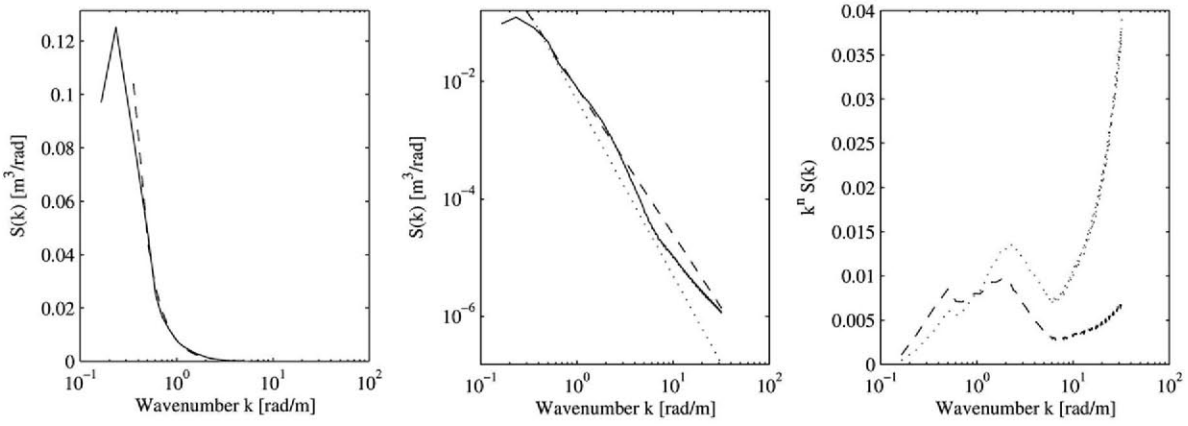

Fig. 11. Experiment 2. Left: wavenumber omnidirectional spectrum in semi log scale. The curves $k^{-2.5}$ (dash line) is superimposed. Center: wavenumber omnidirectional spectrum in log scale. Together with the $k^{-2.5}$ curve (dash line), the k^{-3} curve (dot line) is shown. Right: omnidirectional saturation spectra $k^n S(k)$, with n = 3 (dot line) and n = 2.5 (dash line).

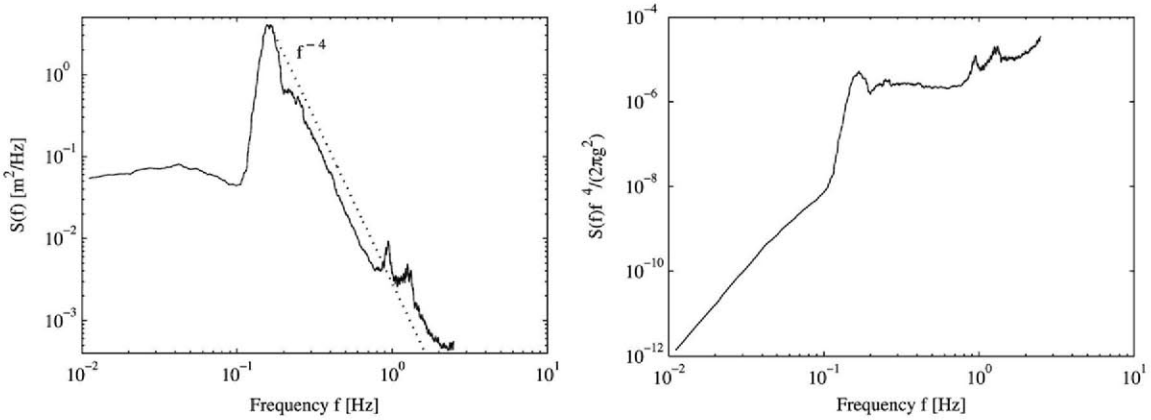

Fig. 12. Experiment 3. Left: Observed mean frequency spectrum $S(f)$ from time series of the surface displacements extracted at 40 virtual probes within the imaged area (see Fig. 9). Nyquist frequency = 2.5 Hz. Right: Associated saturation spectrum $S(f)f^4/(2\pi g^2)$.

$$P(T > h) = \exp\left(-\frac{z^2}{2}(1 + 0.5\mu z)^2\right)\left(1 + \frac{\Lambda}{64}z^2\left(z^2 - 4\right)\right) \tag{14}$$

where $z = h/\sigma$, and Z_c are derived from the quadratic equation $z = Z_c + \mu Z_c^2/2$, with μ as a characteristic parameter that measures wave steepness (Fedele and Tayfun, 2009; Tayfun, 1986), and Λ is a measure of quasi-resonant third order nonlinearities that depends upon the fourth order cumulants of the wave surface η (Tayfun and Fedele, 2007). For our data set $\Lambda \approx 0$, and second order nonlinearities are dominant. The wave steepness μ can be estimated directly from data via time averages as $\mu = <\eta^3>$, where $<>$ denotes statistical expectation. However, these estimators are usually statistically unstable. A stable estimate for "μ follows from the moments of the wave spectrum as (Fedele and Tayfun, 2009)

$$\mu_a = \mu_m\left(1 - \nu + \nu^2\right), \tag{15}$$

with ν as the spectral bandwidth given by

$$\nu = \sqrt{\frac{m_0 m_2}{m_1^2} - 1} \tag{16}$$

where $m_j = \int \omega^j S(\omega) d\omega$ are spectral moments, $\mu_m = \sigma\omega_m^2/g$, and $\omega_m = m_1/m_0$ is the mean up-crossing frequency (Tayfun, 1986). The observed values for these parameters are given by $\mu = 0.067$, $\mu_m = 0.093$, $\mu_a = 0.071$ and $\nu = 0.38$ for Experiment 3. The Forristall model (Forristall, 2000) for crest heigths is given by

$$P(C > z) = \exp\left[-\left(\frac{z}{4\alpha}\right)^{\beta}\right], \tag{17}$$

where the parameters α and β depend upon a steepness S_1 and the Ursell-type number U_r defined, respectively, as

$$S_1 = \frac{2\pi H_S}{gT_m^2}, U_r = \frac{H_S}{d^3 k_m^2} \tag{18}$$

Their observed values from the data set are $S_1 \approx 0.071$ and $U_r \approx 0$. Following Forristall (2000), for unidirectional (2-D) seas $\alpha = \alpha_2 = 0.374$, $\beta = \beta_2 = 1.848$, whereas for multidirectional (3-D) seas $\alpha = \alpha_3 = 0.372$ and $\beta = \beta_3 = 1.874$, and the associated models (17) are labeled as F2 and F3 respectively. The observed crest exceedance is given in Fig. 17. There is fair agreement with both the TF and F, and similar conclusions hold for the observed trough statistics.

Finally, we point out that the discrepancy observed between the theoretical models and the empirical distributions over the extreme tail may possibly be due in part to wave breaking and in part to the stochastic dependence of the time series extracted at the virtual probes, which are too close compared to the mean wavelength.

3. Conclusions and future developments

We have deployed a Wave Acquisition Stereo System (*WASS*) at the oceanographic platform *Acqua Alta* off the Venice coast in Italy. As a video observational technology, *WASS* is able to provide a multi-dimensional image of the oceanic state around the tower. Advanced stereo techniques based on epipolar geometry are exploited to obtain 3-D reconstructions of the sea surface both in space and in time. The accuracy of *WASS* measurements is shown to be comparable to that of more traditional wave instruments. Further, the directional

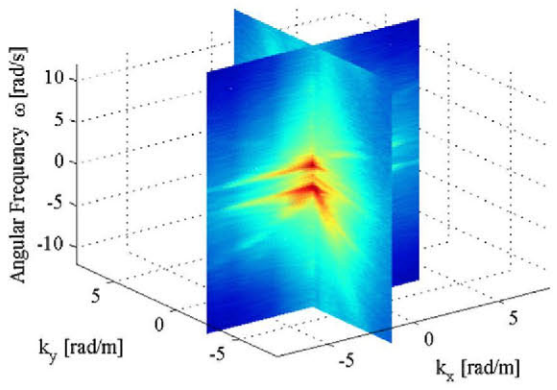

Fig. 13. Experiment 2. Left: Two orthogonal projections (slices) of the wave 3-D spectrum $S(k_x, k_y, \omega)$ onto the planes $k_x = 0$ and $k_y = 0$, respectively.

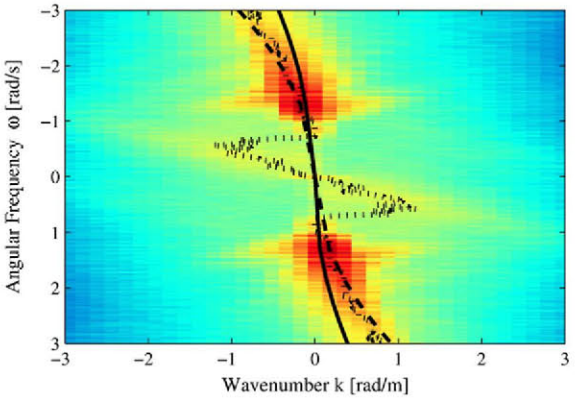

Fig. 14. Experiment 3. 2-D Log spectrum, observed dispersion curve (dot line), theoretical dispersion curve without current (solid line) and with current (dash line).

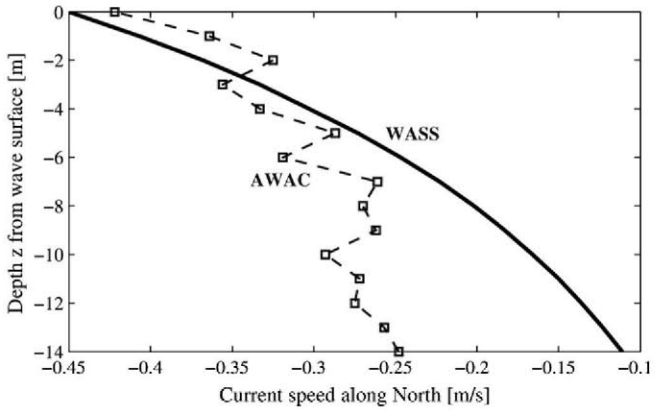

Fig. 15. Experiment 3. AWAC current vertical profile measurements and *WASS* estimates.

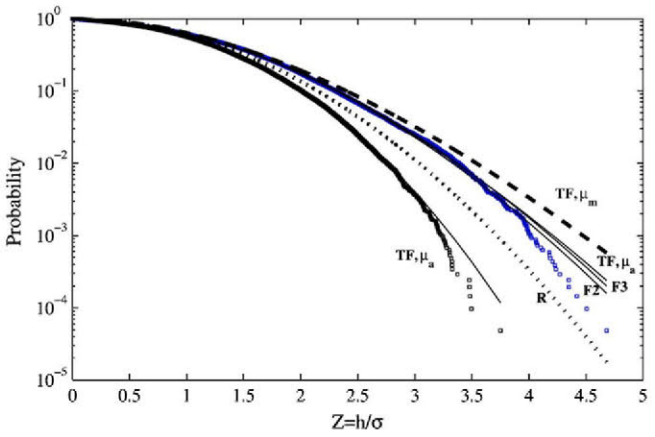

Fig. 17. Experiment 3. Wave crests and troughs exceedance probability. Black (troughs) and blue (crests) dots are from *WASS* data. Superimpose some theoretical distributions: R: Rayleigh; TF: Tayfun-Fedele model with steepness μ; F2: 2-D Forristall; F3: 3-D Forristall.

spectrum is estimated directly by averaging over the reconstructed spatial snapshots, and the 3-D Fourier Transform of the entire space-time data set provides estimates of wave dispersion and currents. In principle, orbital velocities on the surface can be estimated via inversion of the Laplace equation (Grue et al., 2008). The statistics of crest and trough heights, as well as crest-to-trough heights, estimated via *WASS* exhibit fair agreement with known theoretical models such as the Forristall and Tayfun-Fedele distributions for crests and the Boccotti model for wave heights.

In the future, we plan to speed up the stereo reconstruction algorithm by means of Graphics Processing Units (GPU) to compute the Fast Fourier Transform (FFT) efficiently. Preliminary results carried out on a dual-core processor show that the computational time could be reduced by a factor of 10 using standard GPU boards. This will enable the stereo reconstruction of high-resolution images, reducing noise in the space-time data, and extending the accuracy of the computed spectra to higher frequencies and wavenumbers. Finally, GPU-based FFT algorithms will be beneficial for the computation of 3-D wave spectra at high resolution and surface orbital velocities.

We point out that *WASS* reconstructions can be further improved using variational stereo reconstruction methods that exploit the spatial and temporal continuity of the ocean surface (Gallego et al., 2011). Indeed, while epipolar methods return a set of scattered and independent 3-D points of the estimated ocean surface, variational methods provide dense and coherent estimates of both its shape and radiance as minimizers of a composite energy functional that combines a photometric matching term along with regularization terms involving the smoothness of the unknowns. The desired ocean surface shape and radiance follow from the solution of the necessary optimality condition (Euler-Lagrange equation) of the energy functional. We have applied such variational approach to analyze *WASS* measurements taken near the southern seashore of the Crimean peninsula, in the Black Sea (Gallego et al., 2011). In particular, Fig. 18 reports the plot of the estimated mean frequency spectrum (red line). The epipolar-based counterpart (black line) has a peak at 2 Hz, which is most likely due to vibrations induced by fishermen walking on the platform at the time while *WASS* was recording. Since the epipolar reconstruction is based on the imaged data with no form of regularization as in the variational approach, noise induced by uncontrolled environmental factors (as fishermen walking in this case) must be filtered out a posteriori. On the other hand, the variational method appears more robust to noise because the space-time coherence of the ocean surface is embedded into the reconstruction evolution process. In addition, the variational method is not affected by quantization error or gaps/holes due to localized textureless regions. As a result, stereo techniques have the potential to unveil small-scale structures of the sea surface improving estimates of wave spectra at both large wavenumbers and frequencies.

Finally, we bring to the reader's attention that *WASS* is relevant in offshore industry for a proper design of the air gap under the deck of fixed structures. Indeed, localized damages have been observed on the lower decks of platforms after storms (Forristall, 2006, 2007). This may be due to a design of the rig that is based on the expected

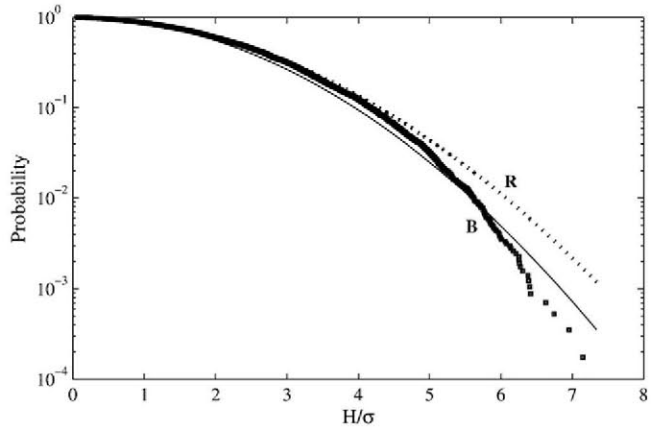

Fig. 16. Experiment 3. Wave height exceedance probability. Rayleigh (R) and Boccotti (B) theoretical distribution are superimposed.

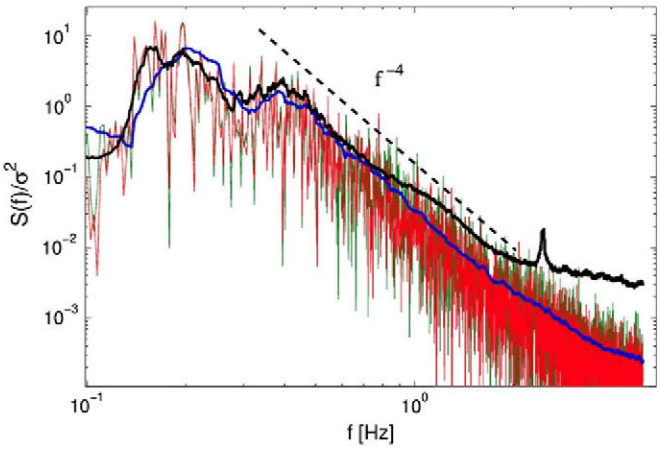

Fig. 18. Crimea experiment: $S(f)$ spectrum estimated using variational methods (blue) and its counterpart using classical epipolar methods (black). The deployed *WASS* includes two BM-200GE JAI cameras (2 mega pixel) with a square cell size of 4.40 μm×4.40 μm, mounting 5-mm focal length low distortion lenses.

largest crest elevation at a given point in time that underestimates the expected largest wave surface elevation over the rig's area footprint. Fedele et al. (2011, 2012) have confirmed such underestimation, in agreement with theoretical predictions based on Piterbarg's theory (Piterbarg, 1996) and Adler's Euler characteristics (Adler, 1981; Adler and Taylor, 2007).

Acknowledgements

Research supported by CASE-EJIP Joint Industry Project (project #4545093). The authors thank Profs. Aziz Tayfun and Harald Krogstad for useful comments and discussions. Protecno S.r.l. and Phoenix S.r.l. helped *WASS* deployment at *Acqua Alta*. A special thanks to Luigi Cavaleri, Mauro Sclavo and Mauro Bastianini that have been involved with the project since the very first stage. The analysis of Crimea video measurements is supported by ONR grant BAA 09-012: "Ocean Wave Dissipation and energy Balance (WAVE-DB): toward reliable spectra and first breaking statistics". The authors also thank Dr. Fabrice Ardhuin for useful discussions on current estimation from wave dispersion curves.

References

Adler, R.J., 1981. The Geometry of Random Fields. John Wiley, New York.
Adler, R.J., Taylor, J.E., 2007. Random Fields and Geometry. Springer Monographs in Mathematics Springer, New York.
Allender, J., Audunson, T., Barstow, S.F., Bjerken, S.H., Krogstad, E., Steinbakke, P., Vartdal, L., Borgman, L.E., Graham, C., 1989. The WADIC project: a comprehensive field evaluation of directional wave instrumentation. Ocean Engineering 16, 505–536.
Banner, M.L., Jones, S.F., Trinder, J.C., 1989. Wavenumber spectra of short gravity waves. Journal of Fluid Mechanics 198, 321–344.
Bechle, A.J., Wu, C.H., 2011. Virtual wave gauges based upon stereo imaging for measuring surface wave characteristics. Coastal Engineering 58 (4), 305–316.
Benetazzo, A., 2006. Measurements of short water waves using stereo matched image sequences. Coastal Engineering 53, 1013–1032.
Blostein, S.D., Huang, T.S., 1987. Error analysis in stereo determination of 3-D point positions. IEEE Transactions on Pattern Analysis and Machine Intelligence 9 (6), 752–765.
Boccotti, P., 2000. Wave Mechanics for Ocean Engineering. Elsevier Science, Oxford.
Cavaleri, L., Bertotti, L., Tescaro, N., 1997. The modelled wind climatology of the Adriatic Sea. Theoretical and Applied Climatology 56, 231–254.
Dankert, H., Horstmann, J., Lehner, S., Rosenthal, W.G., 2003. Detection of wave groups in SAR images and radar image sequences. IEEE Transactionson Geoscience and Remote Sensing 41, 1437–1446.
de Vries, S., Hill, D.F., de Schipper, M.A., Stive, M.J.F., 2011. Remote sensing of surf zone waves using stereo imaging. Coastal Engineering 58 (3), 239–250.
Fedele, F., 2008. Rogue waves in oceanic turbulence. Physica D 237 (14–17), 2127–2131.
Fedele, F., Tayfun, M.A., 2009. On nonlinear wave groups and crest statistics. Journal of Fluid Mechanics 620, 221–239.
Fedele, F., Benetazzo, A., Forristall, G.Z., 2011. Space-time waves and spectra in the Northern Adriatic Sea via a Wave Acquisition System. Proceedings of the ASME 2011 30th International Conference on Ocean, Offshore and Arctic Engineering (OMAE 2011) in Rotterdam, The Netherlands.
Fedele, F., Gallego, G., Yezzi, A., Benetazzo, A., Cavaleri, L., Sclavo, M., Bastianini, M., 2012. Euler characteristics of oceanic sea states. Mathematics and Computers in Simulation 82 (6), 1102–1111.
Forristall, G.Z., 2000. Wave crests distributions: observations and second order theory. Journal of Physical Oceanography 38 (8), 1931–1943.
Forristall, G.Z., 2006. Maximum wave heights over an area and the air gap problem. Proceedings of the ASME 2006 25th International Conference on Ocean, Offshore and Arctic Engineering (OMAE 2006) in Hamburg, Germany.
Forristall, G.Z., 2007. Wave crest heights and deck damage in Hurricanes Ivan, Katrina and Rita. Proceedings of the Offshore Technology Conference Proceedings in Houston, USA.
Gallego, G., Yezzi, A., Fedele, F., Benetazzo, A., 2011. A variational stereo method for the 3-D reconstruction of ocean waves. IEEE Transactions of Geosciences and Remote Sensing 49 (11), 4445–4457.
Goring, D.G., Nikora, V.I., 2002. Despiking acoustic doppler velocimeter data. Journal of Hydraulic Engineering 128, 117–126.
Grue, J., Romero, L., Kleiss, J., Melville, W.K., 2008. Orbital velocity in spatial ocean wave elevation measurement: nonlinear computation and approximation. Proceedings of the ASME 2008 27th International Conference on Ocean, Offshore and Arctic Engineering (OMAE 2008) in Estoril, Portugal.
Heikkila, J., Silven, O., 1997. A four-step camera calibration procedure with implicit image correction. Proceedings of 1997 IEEE Computer Society Conference in San Juan, Puerto Rico.
Holthuijsen, L.H., 1983. Observations of the directional distribution of ocean wave energy. Journal of Physical Oceanography 13, 816–827.
Hwang, P., Wang, D., Walsh, E., Krabill, W., Swift, R., 2000. Airborne measurements of the wavenumber spectra of ocean surface waves, part I: spectral slope and dimensionless spectral coefficient. Journal of Physical Oceanography 30, 2753–2767.
Jahne, B., 1993. Spatio-Temporal Image Processing – Theory and Scientific Applications. Springer-Verlag Berlin Heidelberg.
Kosnik, M.V., Dulov, V.A., 2011. Extraction of short wind wave spectra from stereo images of the sea surface. Measurement Science and Technology 22, 1–10.
Krogstad, H.E., Trulsen, K., 2010. Interpretations and observations of ocean wave spectra. Ocean Dynamics 60 (4), 973–991.
Ma, Y., Soatto, S., Kosecka, J., Shankar Sastry, S., 2004. An invitation to 3-D vision: from images to geometric models. Springer-Verlag New York.
Malanotte-Rizzoli, P., Bergamasco, A., 1983. The dynamics of coastal region of the northern Adriatic Sea. Journal of Physical Oceanography 13, 1105–1130.
Marom, M., Goldstein, R.M., Thornton, E.B., Shemer, L., 1990. Remote sensing of ocean wave spectra by interferometric synthetic aperture radar. Nature 345, 793–795.
Marom, M., Shemer, L., Thornton, E.B., 1991. Energy density directional spectra of nearshore wavefield measured by interferometric synthetic aperture radar. Journal of Geophysical Research 96, 22125–22134.
Newell, A.C., Zakharov, V.E., 2008. The role of the generalized Phillip's spectrum in wave turbulence. Physics Letters A 372 (23), 4230–4233.
Nobach, H., Honkanen, M., 2005. Two-dimensional Gaussian regression for sub-pixel displacement estimation in particle image velocimetry and particle position estimation in particle tracking velocimetry. Experiments in Fluids 38, 511–515.
O'Reilly, W.C., Herbers, T.H.C., Seymour, R.J., Guza, R.T., 1996. A comparison of directional buoy and fixed platform measurements of Pacific swell. Journal of Atmospheric and Oceanic Technology 13, 231–238.
Park, C.S., Park, H.W., 2001. A robust stereo disparity estimation using adaptive window search and dynamic programming search. Pattern Recognition 34 (12), 2573–2576.
Phillips, O.M., 1977. The Dynamics of the Upper Ocean. Cambridge University Press.
Piterbarg, V., 1996. Asymptotic Methods in the Theory of Gaussian Processes and Fields. American Mathematical Society, Providence, RI.
Rodriguez, J.J., Aggarwal, J.K., 1990. Stochastic analysis of stereo quantization error. IEEE Transactions on Pattern Analysis and Machine Intelligence 12 (5), 467–470.
Shemdin, O.H., Tran, H.M., Wu, S.C., 1988. Directional measurements of short ocean waves with stereography. Journal of Geophysical Research 93, 13891–13901.
Solina, F., 1985. Errors in stereo due to quantization. Dep. Comput. Inform. Sci., Univ. Pennsylvania, Philadelphia, Tech. Rep. MS-CIS-85-34.
Stewart, R.H., Joy, J.W., 1974. HF radio measurements of surface currents. Deep Sea Research 21 (12), 1039–1049.
Tayfun, M.A., 1986. On narrow-band representation of ocean waves. Part I: Theory Journal of Geophysical Research 1 (C6), 7743–7752.
Tayfun, M.A., Fedele, F., 2007. Wave-height distributions and nonlinear effects. Ocean Engineering 34 (11–12), 1631–1649.
Tombari, F., Mattoccia, S., Di Stefano, L., Addimanda, E., 2008. Classification and evaluation of cost aggregation methods for stereo correspondence. Proceedings of IEEE International Conference on Computer Vision and Pattern Recognition (CVPR 2008), June 24–26, 2008, Anchorage, Alaska.
Wanek, J.M., Wu, C.H., 2006. Automated trinocular stereo imaging system for three-dimensional surface wave measurements. Ocean Engineering 33 (5–6), 723–747.
Zakharov, V.E., 1999. Statistical theory of gravity and capillary waves on the surface of a finite-depth fluid. European Journal of Mechanics - B/Fluid 18 (3), 327–344.
Zhang, Z., 2000. A flexible new technique for camera calibration. IEEE Transactions on Pattern Analysis and Machine Intelligence 22 (11), 1330–1334.